Hydraulic properties of closely-spaced dipping open fractures intersecting a fluid-filled borehole derived from tube-wave generation and scattering: Dipping fractures from tube waves

Minato, Shohei; Ghose, Ranajit; Tsuji, Takeshi; Ikeda, Michiharu; Onishi, Kozo

DOI
10.1002/2017JB014681

Publication date
2017

Document Version
Final published version

Published in
JGR Solid Earth

AGU PUBLICATIONS

JGR

Journal of Geophysical Research: Solid Earth

RESEARCH ARTICLE
10.1002/2017JB014681

Key Points:
- A new, extended model for tube wave generation and scattering at closely spaced, dipping, open fractures
- Significance of fracture dip to tube wave reflection coefficients, generation amplitudes and the focusing analysis
- Tube wave synthetic and field data present new evidences and so far unresolved fracture properties

Supporting Information:
- Supporting Information S1
- Data Set S1

Correspondence to:
S. Minato,
s.minato-1@tudelft.nl

Citation:
Minato, S., Ghose, R., Tsuji, T., Ikeda, M., & Onishi, K. (2017). Hydraulic properties of closely spaced dipping open fractures intersecting a fluid-filled borehole derived from tube wave generation and scattering. *Journal of Geophysical Research: Solid Earth*, *122*. https://doi.org/10.1002/2017JB014681

Received 7 JUL 2017
Accepted 17 SEP 2017
Accepted article online 22 SEP 2017

Hydraulic Properties of Closely Spaced Dipping Open Fractures Intersecting a Fluid-Filled Borehole Derived From Tube Wave Generation and Scattering

Shohei Minato[1], Ranajit Ghose[1], Takeshi Tsuji[2,3], Michiharu Ikeda[4], and Kozo Onishi[5]

[1]Department of Geoscience and Engineering, Delft University of Technology, Delft, Netherlands, [2]Department of Earth Resources Engineering, Kyushu University, Fukuoka, Japan, [3]International Institute for Carbon-Neutral Energy Research, Kyushu University, Fukuoka, Japan, [4]Shikoku Research Institute Inc., Takamatsu, Japan, [5]Shikoku Electric Power Co. Inc., Takamatsu, Japan

Abstract Fluid-filled fractures and fissures often determine the pathways and volume of fluid movement. They are critically important in crustal seismology and in the exploration of geothermal and hydrocarbon reservoirs. We introduce a model for tube wave scattering and generation at dipping, parallel-wall fractures intersecting a fluid-filled borehole. A new equation reveals the interaction of tube wavefield with multiple, closely spaced fractures, showing that the fracture dip significantly affects the tube waves. Numerical modeling demonstrates the possibility of imaging these fractures using a focusing analysis. The focused traces correspond well with the known fracture density, aperture, and dip angles. Testing the method on a VSP data set obtained at a fault-damaged zone in the Median Tectonic Line, Japan, presents evidences of tube waves being generated and scattered at open fractures and thin cataclasite layers. This finding leads to a new possibility for imaging, characterizing, and monitoring in situ hydraulic properties of dipping fractures using the tube wavefield.

1. Introduction

Subsurface fractures are of great interest in seismology and in hydrocarbon and geothermal exploration, as they play a crucial role in determining the fluid flow and deformation processes in rocks. In order to characterize hydraulic properties of fractures intersecting a borehole, low-frequency Stoneley waves (tube waves) propagating along a fluid-filled borehole have been studied extensively in the past (e.g., Beydoun et al., 1985). Contrary to indirect measurements (e.g., borehole televiewer), the tube waves sense directly the hydraulic properties of the individual fractures, because these waves induce fluid exchange between the borehole and the fracture. Tube waves can provide in situ permeability corresponding to micrometer- to millimeter-scale fractures (e.g., Hardin et al., 1987; Hornby et al., 1989), as well as the permeability of larger-scale (cm to m) geological faults (e.g., Li et al., 1994; Kiguchi et al., 2001).

Hydraulic fractures are generally characterized using two different attributes of tube waves: (1) scattering (reflection and transmission) of tube waves (Hornby et al., 1989; Kostek et al., 1998; Tang & Cheng, 1993) and (2) tube wave generation amplitudes (Bakku et al., 2013; Beydoun et al., 1985; Cicerone & Toksöz, 1995; Ionov, 2007; Hardin et al., 1987; Li et al., 1994). The first attribute is caused by the pressure perturbation at the fracture-borehole intersection, which is characterized in terms of the reflection and transmission coefficients. The second attribute is observed in a vertical seismic profiling (VSP) due to the deformation of the fracture by an incident *P* wave, which is evaluated using the generated amplitudes and the incident wave.

These conventional approaches assume the tube waves to be generated and scattered by a single fracture. They cannot characterize closely spaced multiple fractures, because it is difficult to isolate tube waves from each individual fracture. In order to overcome this problem, a novel use of the representation theorem, which correctly predicts the interaction of tube waves due to multiple fractures, has recently been proposed (Minato & Ghose, 2017). However, this previous study considers only horizontal fractures. In the present research, we make a major extension of this approach in order to include the effects of the dip of the fracture. Analyzing the

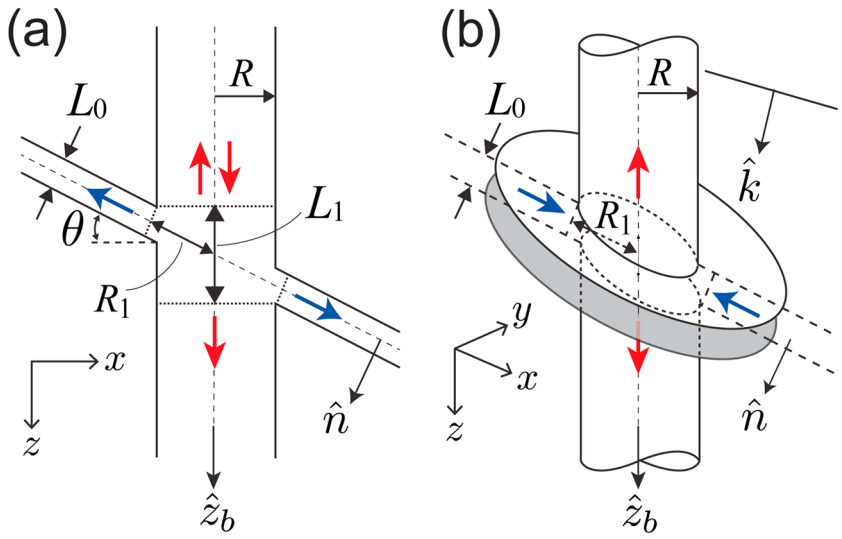

Figure 1. Fracture model in this study. A dipping fracture with aperture L_0 and normal vector $\hat{n}$ intersects a borehole with radius R and unit vector $\hat{z}_b$. (a) Downgoing transmitted and upgoing reflected tube waves (red arrows) are generated due to the incident tube wave and fluid flow into the fracture (blue arrows). $\theta = \cos^{-1}(\hat{z}_b \cdot \hat{n})$ denotes the dip angle and L_1 the vertical extent of the fracture. R_1 is the semimajor axis of the fracture-borehole boundary. (b) An incident P wave with wave number unit vector $\hat{k}$ deforms the fracture, causes the fluid flow (blue arrows), and generates tube waves (red arrows).

effects of the dip angle is critical to characterizing closely spaced multiple fractures, such as a fault-damaged zone, because the dip angles depend on the principle slip direction (Segall & Pollard, 1983). Also, the permeability structure due to dipping fractures controls the deformation processes within the crust (Wibberley & Shimamoto, 2003).

Here we first review briefly the existing theories for tube wave scattering and generation using a parallel-wall open fracture model before presenting a new model for dipping fractures. Contrary to earlier studies that considered dipping fractures (e.g., Beydoun et al., 1985; Hornby et al., 1989; Li et al., 1994; Tang & Cheng, 1993), our new model captures the simultaneous effects of dip angles, dynamic fluid flow, fracture apertures, and fracture compliances. We then use this model to illustrate the interaction of total tube wavefield with dipping fractures, including multiple tube wave generation and scattering. The correct prediction of the total tube wavefield due to closely spaced dipping fractures, and imaging and characterization of these fractures have not been possible so far. Our calculated reflection coefficient and effective tube wave generation amplitude reveal the significance of dip angles. We perform realistic numerical modeling of the complex signature of the total tube wavefield due to multiple dipping fractures. As conventional approaches are not feasible, we propose a focusing analysis for imaging and characterizing dipping fractures. Finally, we test the new method on a VSP data set obtained at a fault-damaged zone located on the Median Tectonic Line, Shikoku, Japan, where closely spaced dipping fractures are dominant features. Understanding this zone is crucial in the assessment of deformation associated with plate subduction.

2. Review of Existing Tube Wave Models: Comparison With a Newly Proposed Model

The generation and scattering of tube waves is a solid-fluid coupling problem where a fluid-filled fracture intersecting a borehole deforms and causes a fluid flow (Figure 1). In order to show the differences and the link between the earlier models and a newly proposed one (this research), we briefly review the theories for a parallel-wall open fracture developed so far.

2.1. Tube Wave Generation Models

The tube wave generation models provide the analytical amplitude of the generated tube waves. In order to derive the amplitude, they generally consider the following procedure; (1) the closure of the fracture wall (dynamic aperture) is defined from the interaction of the incident plane P wave, (2) using the dynamic aperture, the fluid pressure distribution in the fracture is solved using the equation of continuity for fluid,

Table 1
Classification of Tube Wave Generation Models by Formulation of Dynamic Aperture, Fluid Flow Condition, Consideration of Dip Angles, and the Boundary Condition at the Fracture-Borehole Intersection

Model	Formulation of dynamic aperture	Fluid flow condition	Dip angle	Boundary condition
Beydoun et al. (1985)	Displacement	Darcy's law	Dipping	Beydoun BC
Hardin et al. (1987)	Stress	Darcy's law	Dipping	Beydoun BC
Ionov (2007)	Displacement	Low-/high-frequency approximation	Horizontal	Ionov BC
Bakku et al. (2013)	Stress	Dynamic flow	Horizontal	Ionov BC
This research	Stress	Dynamic flow	Dipping	Ionov BC

and (3) the rate of volumetric fluid flow into the borehole is obtained from the pressure distribution, which determines the amplitude of the tube waves. The various models developed so far can be classified by the formulation of dynamic aperture, the fluid flow condition, the consideration of dipping structures, and the boundary condition at the fracture-borehole intersection (Table 1).

We begin with the formulations for the dynamic aperture given in Hardin et al. (1987), viz., displacement and stress formulations (Table 1). Beydoun et al. (1985) first consider the displacement formulation assuming the dynamic aperture to be equal to the displacement amplitude of the incident *P* wave. Ionov (2007) later derives the dynamic aperture by solving the scattering problem of the incident wave interacting with a three-layered model (a fracture embedded in homogeneous background). The dynamic apertures derived from both models are laterally invariant along a fracture. We classify such models as the displacement formulation. This formulation is independent of the presence of the borehole. On the contrary, the stress formulation assumes the aperture to be linked to the fluid pressure through the effective stress (Bakku et al., 2013; Hardin et al., 1987). The dynamic aperture in this case is laterally varying, because of the presence of the borehole and the boundary condition at the fracture-borehole intersection. A suitable formulation for the dynamic aperture is still under debate. However, a recent model proposed by Bakku et al. (2013) exploits the advantage of the stress formulation; it can handle the effect of fracture compliance, for example, roughness of the fracture surface.

Earlier models consider Darcy's law (Table 1) incorporating the effect of the static permeability and fluid viscosity. The recent models, on the other hand, consider a high-frequency approximation (Ionov, 2007) where the propagation mode is dominant in the fracture. Bakku et al. (2013) consider the dynamic fluid flow condition using the frequency-dependent permeability of a rigid fracture (Tang & Cheng, 1989), which is valid over a wide range of frequencies.

Two different boundary conditions (BC) have been proposed at the fracture-borehole intersection. The earlier models assume that the fluid pressure perturbation at the boundary is negligibly small, which we call the Beydoun boundary condition (Table 1). Ionov (2007) later considers a more realistic boundary condition in which the pressure at the boundary is equal to the amplitude of the generated tube wave (the Ionov boundary condition). Recently, Minato and Ghose (2017) have derived the representation theorem for tube waves and have shown that the Ionov boundary condition is equivalent to considering additional scattering to be taking place immediately after the generation, which is caused by the Beydoun boundary condition. Note that Minato and Ghose (2017) have used the model of Bakku et al. (2013). However, the representation theorem derived by Minato and Ghose (2017) can incorporate any model developed so far.

The effect of dip angle is considered only in the models of Beydoun et al. (1985) and Hardin et al. (1987) (see Table 1). Contrary to the dipping fracture models in the tube wave scattering problem which we discuss later in section 2.2, the models of Beydoun et al. (1985) and Hardin et al. (1987) do not consider the effect of the elliptical fracture-borehole intersection (see Figure 1). Due to the wide range of advantages (e.g., handling dynamic flow, the Ionov boundary condition, and the fracture compliance), in the present study we consider the model developed by Bakku et al. (2013) and extend this model to dipping fractures by introducing the effect of the elliptical fracture-borehole intersection (Table 1). In order to achieve this goal, we employ the equivalent circle approach which is first proposed in the tube wave scattering problem by Tang and Cheng (1993). We will explain this approach in sections 2.2 and 3.

Table 2
Classification of Tube Wave Scattering Models by Fluid Flow Condition, Consideration of Dip Angles, and Fracture Compliance

Model	Fluid flow condition	Dip angle	Fracture compliance
Hardin et al. (1987)	Darcy's law	Horizontal	Rigid
Hornby et al. (1989)	Low-/high-frequency approximation	Dipping (elliptical coordinate)	Rigid
Tang and Cheng (1993)	Low-/high-frequency approximation	Dipping	Rigid
Bakku et al. (2013)	Dynamic flow	Horizontal	Compliant
This research	Dynamic flow	Dipping	Compliant

2.2. Tube Wave Scattering Models

The tube wave scattering problem considers the fluid flow due to the pressure perturbation at the fracture-borehole intersection (Figure 1a). The mass conservation equation across the fracture is used to derive the reflection and transmission coefficients. We classify the existing models in terms of fluid flow condition, consideration of dip angles and that of the compliant fracture (Table 2).

Hardin et al. (1987) describe this problem for a rigid, horizontal fracture. Hornby et al. (1989) later extend the theory using low-/high-frequency approximation for dipping fractures. They consider the elliptical fracture-borehole intersection and solve the scattering problem in elliptical coordinate system, which gives analytical solutions containing Mathieu functions. Tang and Cheng (1993) propose a simple alternative approach replacing elliptic cylinder boundary by circular cylinder one with the circle radius equivalent to the circumference of the elliptical boundary (see section 3 for details).

Bakku et al. (2013) use the same equation of continuity as that in their tube wave generation model and derive the transmission coefficient considering dynamic fluid flow condition and the effect of fracture compliance. As we explain earlier, we use the model from Bakku et al. (2013) and extend it to dipping fractures (Table 2).

It is worthwhile to mention that Kostek et al. (1998) extend the theory of Hornby et al. (1989) to include the elasticity of the fracture wall. Therefore, their model also considers dipping, compliant fractures. However, this model is not same as that of Bakku et al. (2013). The model of Kostek et al. (1998) assumes the Stoneley wave mode in the fracture to be one which is obtained from Ferrazzini and Aki (1987), which, in turn, is derived from the boundary conditions at the interface between a nonviscous fluid and an elastic solid. On the other hand, the model of Bakku et al. (2013) considers that the Stoneley wave wave number is obtained from the boundary conditions for a rigid fracture which is filled with a viscous fluid (Tang & Cheng, 1989), and that the wave number is modified due to the fracture compliance, using the equation of continuity (see equation 5 in Bakku et al., 2013). The Stoneley wave mode considered in Kostek et al. (1998) is closely related to the Krauklis waves (e.g., Ashour, 2000; Lipovsky & Dunham, 2015). The one considered in Bakku et al. (2013) corresponds to the Biot slow wave (e.g., Biot, 1956). The differences and the relation between these two modes are discussed in Koorneev (2008).

3. Theory

3.1. Total Tube Wavefield Due to Multiple Fractures

In a fluid-filled borehole embedded in an elastic medium, the Stoneley wave mode dominates at low frequencies or large wavelengths (Biot, 1952). Therefore, solving the one-dimensional equation is sufficient for evaluating tube wave propagation (Tezuka et al., 1997). From the quasi-static wave approximation (White, 1983), the equation of motion and the constitutive relation are represented by vertical particle velocity (v_z) and acoustic pressure (p). The impulse responses (Green's functions) are characterized by the tube wave velocity $c_T = (\rho_f^{-1} K_{\text{eff}})^{1/2}$, where ρ_f is the fluid density and K_{eff} the effective fluid bulk modulus (Chang et al., 1988; White, 1983).

Recently, Minato and Ghose (2017) have discussed the interaction of total tube wavefield with multiple fractures. This is a one-dimensional multiple scattering problem involving scalar waves due to multiple,

simultaneously acting sources. By exploiting the representation theorem, the total tube wave pressure field (p) can be derived as a function of the tube wave generation potential (ϕ_g) and scattering potential (ϕ_s):

$$p(z,\omega) - p_{\mathrm{inc}}(z,\omega) = \int_{-\infty}^{+\infty} \phi_g(z',\omega)\bar{G}^{pq}(z,z',\omega)p_{\mathrm{inc}}(z',\omega)\mathrm{d}z' + \int_{-\infty}^{+\infty} \phi_s(z',\omega)\bar{G}^{pq}(z,z',\omega)\left[p(z',\omega) - p_{\mathrm{inc}}(z',\omega)\right]\mathrm{d}z', \tag{1}$$

where p_{inc} is the pressure field due to the incident plane P wave, and $\bar{G}^{pq}(z,z',\omega)$ is the Green's function in the reference medium at z due to a point source at z'. The tube wave potential functions (ϕ_g and ϕ_s) contain the hydraulic properties of the dipping fractures, that is, $\phi_g(z,\omega) = \sum_{i=1}^{N}(\rho_f c_T/2)^{-1}\gamma_g^{(i)}\delta(z-z_i)$ and $\phi_s(z,\omega) = i\omega\sum_{i=1}^{N}\eta^{(i)}\delta(z-z_i)$, where N fractures are located at z_i ($i = 1, 2, \ldots, N$), $\eta^{(i)}$ is the interface compliance, and $\gamma_g^{(i)}$ is the tube-to-P wave amplitude ratio. Here the interface compliance (η) and the tube-to-P wave amplitude ratio (γ_g) are derived for dipping fractures in the following subsections. Equation (1) shows the interaction among total pressure field, incident wave, and hydraulic fractures in terms of the potential functions. This gives us a novel possibility for characterizing multiple hydraulic fractures using tube waves.

Note that equation (1) is obtained from the representation theorem of wave equation including nonwelded interfaces (Wapenaar, 2007), by considering the relation between Green's functions with and without the fractures and by superposing actual Green's functions with the amplitude determined from the tube-to-P wave amplitude ratio (Minato & Ghose, 2017). Equation (1) has the same form as in the previous study. However, here the potential functions (ϕ_g and ϕ_s) contain new information on the dip angles.

3.2. Tube Wave Scattering and Nonwelded Interface Model for Dipping Fractures

We assume that a dipping fracture with an aperture L_0 intersects a borehole with the borehole radius R (Figure 1a). Due to the pressure perturbation at the fracture-borehole intersection, propagating tube waves are reflected and transmitted at the fracture. The key physical mechanism to derive wave scattering at a dipping fracture is mass conservation in the borehole across the fracture. Tang and Cheng (1993) derive this across a dipping fracture in terms of the particle velocity in the fluid $v_z(z,\omega)$:

$$\pi R^2\left\{v_z(-L_1/2,\omega) - v_z(+L_1/2,\omega)\right\} - L_e\, q_f\big|_{r=\bar{R}} = 0, \tag{2}$$

where the fracture is assumed to be located at $z = 0$, L_e the circumference of the elliptical fracture-borehole boundary, $\bar{R}$ the radius of an equivalent circle representing this elliptical boundary (Tang & Cheng, 1993), and L_1 the vertical extent of the fracture within the borehole (see Figure 1a). Note that L_e and $\bar{R}$ are calculated from the semiminor axis R and the semimajor axis R_1 of the ellipse, which depend on the dip angle (θ), see Figure 1a and Tang and Cheng (1993) for details. Here the fluid volume into the fracture (blue arrows in Figure 1a) can be calculated as the flow rate $q_f(r,\omega)$ multiplied by the circumference of fracture-borehole boundary (L_e), where r is the radial distance, evaluated at the effective fracture-borehole intersection ($r = \bar{R}$). In order to evaluate more correctly the fluid volume due to an elliptical fracture-borehole boundary (corresponding to the term $L_e\, q_f\big|_{r=\bar{R}}$ in equation (2), Hornby et al. (1989) solve the scattering problem considering elliptic-cylindrical coordinates and obtain the solutions in the series of radial and angular Mathieu functions. In this study, however, we follow a simple alternative approach as proposed in Tang and Cheng (1993) which considers circular-cylindrical coordinates and the equivalent circle radius, as explained above.

Note that we ignore the additional effect of the dynamic compression of ΔV (a cylinder of height L_1 with a radius R) in equation (2), which is discussed in Tang and Cheng (1993). They show that this effect is generally not significant when the vertical extent L_1 is small compared to the wavelength of tube waves. This assumption is also employed in foregoing studies of dipping fractures (Hornby et al., 1989). Tang and Cheng (1993) derive the term containing the dynamic compression of ΔV assuming that only a single fracture is located within the vertical extent L_1, which is not always the case for closely spaced multiple fractures that we consider in this research. For all these reasons, we ignore the effect of the dynamic compression of ΔV.

Considering q_f from Bakku et al. (2013) allows us to obtain a new model including the simultaneous effects of dip angles, dynamic fluid flow, fracture apertures, and fracture compliances. In this case, q_f is calculated from the mass conservation in the fracture, assuming a viscous fluid in an infinitely long, rigid fracture, and the axial

symmetry of the problem. Exploiting equation 14 in Bakku et al. (2013), equation (2) results in the following boundary condition at the fracture:

$$\Delta v_z = i\omega\eta p, \tag{3}$$

where Δv_z is a discontinuity in the particle velocity across the fracture. Interface compliance η contains the hydraulic properties of the fracture including the effect of the dip angle:

$$\eta = -2\zeta \frac{\bar{R}}{R^2} \frac{L_0}{k_r^2 \alpha_f^2 \rho_f} \frac{H_1(\zeta\bar{R})}{H_0(\zeta\bar{R})}, \tag{4}$$

where α_f is the acoustic velocity of the fluid, ζ is the effective radial wave number ($\zeta = k_r\alpha_f/\alpha_{\text{eff}}$), α_{eff} is the effective fluid velocity in the fracture ($\alpha_{\text{eff}}^{-2} = \alpha_f^{-2} + \rho_f Z/L_0$), Z is the fracture compliance (m/Pa), $H_n = H_n^{(1)}$ is a Hankel function of the first kind and order n, and we use the relation $L_e = 2\pi\bar{R}$. Note that Z is generally a complex function of roughness of the fracture surface, the distribution of contact area, and the elasticity of the material filling the aperture (e.g., Worthington & Lubbe, 2007). Bakku et al. (2013) and Hardin et al. (1987) consider Z to be an independent parameter. In this research, we assume Z to be linked to the fracture aperture (L_0) considering the quasi-static condition of a thin layer of water without asperities, that is, $Z \approx L_0/\rho_f\alpha_f^2$ (e.g., Minato & Ghose, 2016; Nagy, 1992; Rokhlin & Wang, 1991).

Equation (3) represents the key boundary condition in order to discuss the interaction of tube waves with dipping fractures. We further assume that the pressure is continuous across the fracture, that is, $\Delta p = 0$, due to the large wavelength (e.g., Bakku et al., 2013; Hornby et al., 1989). Equation (3) with the continuity of pressure is equivalent to the linear slip boundary condition for a nonwelded interface (e.g., Nagy, 1992; Pyrak-Nolte et al., 1990; Schoenberg, 1980).

Once we obtain the interface compliance η, we can calculate theoretical reflection/transmission coefficients (e.g., Appendix B in Minato & Ghose, 2017), which is also useful in controlled Stoneley wave measurements (e.g., Hornby et al., 1992). We calculate the theoretical reflection coefficient for a dipping ($\theta = 45°$), water-filled fracture with the static aperture $L_0 = 1$ mm (red line in Figure 2a). Here the borehole radius R is 7.5 cm. In order to compare the new model with the foregoing studies of rigid fractures (Hornby et al., 1989; Tang & Cheng, 1993), we assume the fracture compliance (Z) to be zero in Figure 2a. The black lines (solid and dashed black lines) and the symbols (squares and circles) in Figure 2a show, respectively, the results of Hornby et al. (1989) which contain the series of Mathieu functions, and those of Tang and Cheng (1993) which use the equivalent circle approach that we employ in this research. We evaluate the high-frequency (HF, solid black line and open squares in Figure 2a) and low-frequency (LF, dashed black line and open circles in Figure 2a) approximate solutions for these two theories. Note that the results of Hornby et al. (1989) and Tang and Cheng (1993) almost coincide. Our model shows correct limits at low and high frequencies. Figures 2b and 2c show the reflection coefficients for various dip angles in the frequency range that we consider in the numerical modeling section (section 4) and in the field data example (section 5). One can see that the increase of dip angles increases the reflection coefficients. Our model shows smaller reflection coefficients than those obtained from high-frequency approximation (Hornby et al., 1989), mainly due to the effect of fluid viscosity (Figure 2b). We check the effect of the fracture aperture (L_0) in the reflection coefficients (Figure 2d). One can see that the coefficient increases as the fracture aperture increases, which is shown also in the previous studies on horizontal fractures (Bakku et al., 2013) and dipping fractures using high-/low-frequency approximations (Hornby et al., 1989).

3.3. Tube Wave Generation Amplitude for Dipping Fractures

We assume that the incident P wave generates a fluid pulse into the borehole (Figure 1b). From Ionov (2007) and references therein, the tube wave amplitude (p_t) is defined as the rate of fluid volume change ($\mathrm{d}V/\mathrm{d}t$) scaled by the medium parameters and the borehole radius (R):

$$p_t(t) = \frac{\rho_f c_T}{2\pi R^2} \frac{\mathrm{d}V}{\mathrm{d}t}. \tag{5}$$

Considering the elliptical fracture-borehole boundary for a dipping fracture (Figure 1b) and the equivalent circle approach of Tang and Cheng (1993), the following relation can be obtained:

$$\frac{\mathrm{d}V}{\mathrm{d}t} \approx -L_e q_f\big|_{r=\bar{R}}, \tag{6}$$

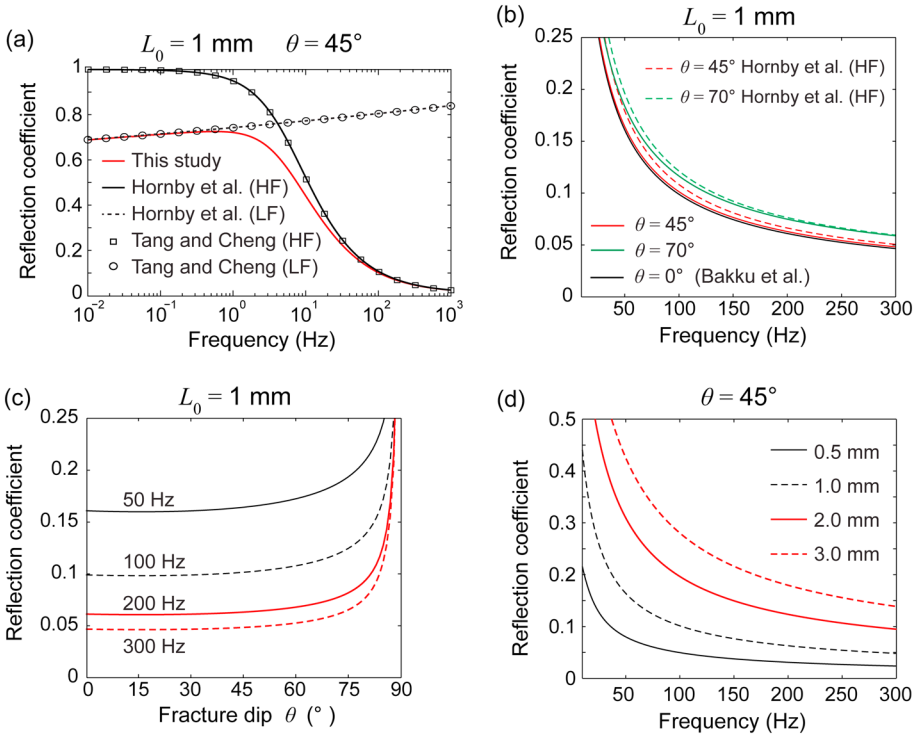

Figure 2. (a) Theoretical reflection coefficients (absolute values) for a 1 mm thick, water-filled, rigid fracture with a 45° dip angle. Results from three models are shown: the new model developed in this study (red line), the model developed by Hornby et al. (1989) containing the series of Mathieu functions (solid and dashed black lines), and the model developed by Tang and Cheng (1993) considering the equivalent circle approach (open squares and circles) that we also employ in this study. Solid black line and open squares indicate high-frequency approximations (HF), and dashed black line and open circles low-frequency approximations (LF). (b) Same as Figure 2a but for different dip angles (θ) in the frequency range that we consider in the numerical modeling and in the field data example. (c) Same as Figure 2b but derived from the present model for different fracture dips (θ) but constant frequencies (50, 100, 200, and 300 Hz). (d) Same as Figure 2b but derived from the present model for different fracture apertures (L_0) but a constant fracture dip (45°).

Equation (6) indicates that the volume injection rate (dV/dt) can be calculated as the volume rate of fluid coming out of the fracture ($-L_e\, q_f\big|_{r=\bar{R}}$). Similar to the scattering model, taking q_f from Bakku et al. (2013) leads us to a new generation model. To derive q_f we follow this approach, but using the Beydoun boundary condition (Beydoun et al., 1985) which states that the generated tube wave does not perturb the pressure in the borehole. Note that a more realistic boundary condition for nonzero pressure perturbation in a borehole (the Ionov boundary condition, Ionov, 2007) is discussed later.

We obtain the amplitude of the generated tube wave due to the dipping fracture as

$$p_t(\omega) = \sigma_0 \frac{L_e}{2\pi R} \frac{i\omega c_T}{k_r \alpha_f} \frac{\rho_f Z \alpha_{\text{eff}}}{R} \frac{H_1(\zeta \bar{R})}{H_0(\zeta \bar{R})}, \tag{7}$$

where σ_0 is stress amplitude of the incident plane P wave acting normal to the fracture. Equation (7) is the new model of tube wave generation due to dipping fractures. Terms containing L_e or $\bar{R}$ in equation (7) represent the effect of the dip angle. For a horizontal fracture ($L_e = 2\pi R$ and $\bar{R} = R$), equation (7) converges to the model developed earlier by Bakku et al. (2013), but using the Beydoun boundary condition (Minato & Ghose, 2017).

In order to eliminate the effect of σ_0 in equation (7), it is convenient to derive further the tube-to-P wave amplitude ratio, that is, $\gamma_g = p_t/p_{\text{inc}}$, where p_{inc} is the incidence pressure in the borehole due to the P wave. Here we consider p_{inc} due to three-dimensionally propagating plane P wave derived from the quasi-static approximation (Hardin et al., 1987; White, 1983).

Next, we will show that the use of equation (1) gives correct amplitude for the generated tube wave at a single fracture, which is observed effectively at a receiver location. The effective amplitude can be obtained

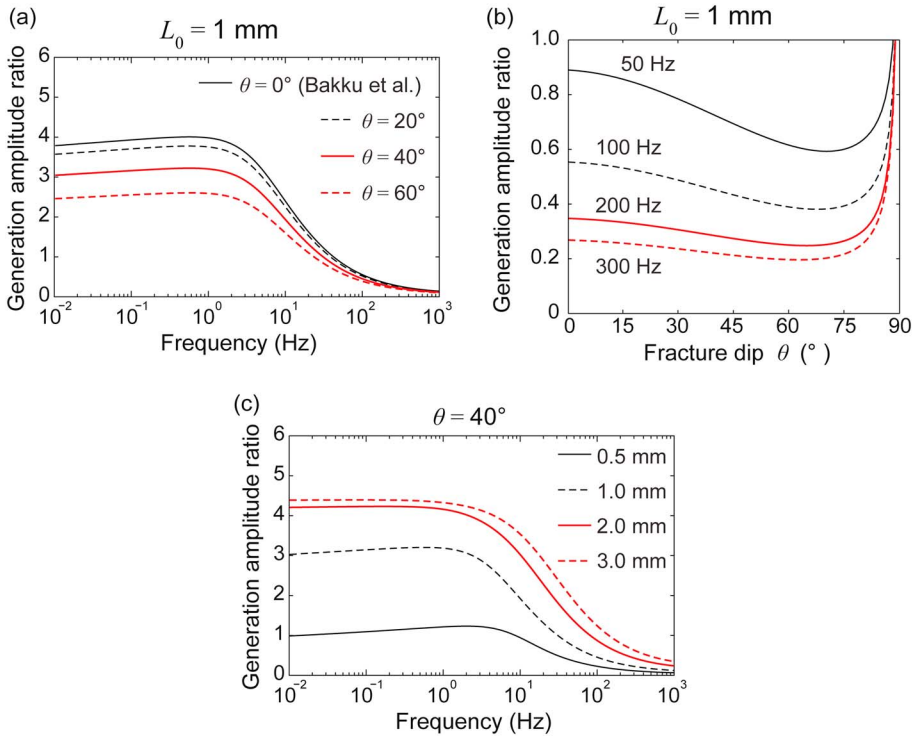

Figure 3. (a) Effective generation amplitude ratio ($p_t^{\text{eff}}/p_{\text{inc}}$) for different fracture dips (θ) with $L_0 = 1$ mm. (b) Same as Figure 3a but for different fracture dips (θ) at constant frequencies (50, 100, 200, and 300 Hz). (c) Same as Figure 3a but for different fracture aperture (L_0) with $\theta = 40°$.

by substituting the potential functions (characterized by η and γ_g) in equation (1) and deriving the amplitude at a receiver location (Minato & Ghose, 2017). Finally, we obtain the following equation:

$$p_t^{\text{eff}} = \frac{p_t}{1 - i\omega\eta\left(\rho_f c_T/2\right)}. \tag{8}$$

Equation (8) shows that the effective amplitude (p_t^{eff}) is connected to the interface compliance (η) of the same fracture or the nonwelded interface, suggesting that the tube wave is scattered immediately after generation. In the case of a horizontal fracture, Minato and Ghose (2017) have shown that the effective amplitude is identical to that obtained using a more realistic boundary condition in which the pressure at the fracture-borehole intersection is equal to the amplitude of the generated tube wave (Ionov boundary condition). Equivalently, the effective amplitude for a dipping fracture (equation (8)) is also identical to that obtained using the Ionov boundary condition (see Appendix A).

We can calculate the effective tube-to-*P* wave amplitude ratio using equation (8), for various dip angles (Figure 3a). We consider here normal incidence plane *P* wave and that a fracture with an aperture $L_0 = 1$ mm intersects a water-filled borehole with radius $R = 7.5$ cm, embedded in the formation ($V_P = 4,500$ m/s, $V_S = 2,200$ m/s, and $\rho = 2,500$ kg/m^3). In this case, the tube wave velocity (c_T) is 1,377 m/s, which is calculated from $c_T = \alpha_f / \sqrt{1 + \rho_f \alpha_f^2 / \rho V_S^2}$ (White, 1983). The results for a horizontal fracture (solid black line in Figure 3a) correspond to the theory developed by Bakku et al. (2013). Figure 3b shows the amplitude ratio for various dip angles at given frequencies (50, 100, 200, and 300 Hz) that are in the frequency range considered in the numerical modeling section and in the field data example. Figures 3a and 3b show that the amplitude ratio decreases with the dip angle until around $\theta = 70°$. This suggests that for our configurations, the fracture normal stress, which becomes small at large dip angles (Hardin et al., 1987), has a greater influence on the generation amplitude ratio than the length of the fracture-borehole boundary, which is large at large dip angles (L_e in equation (7)). At a dip angle larger than 80°, the amplitude ratio rapidly increases with the fracture dip, as can be seen in Figure 3b. This is possibly due to the effect of large values of L_e. Note that when the dip angle is close to 90°, the proposed theory does not accurately predict the amplitude ratio because the vertical extent of the fracture (L_1) is very large compared to the wavelength of tube waves (see section 6).

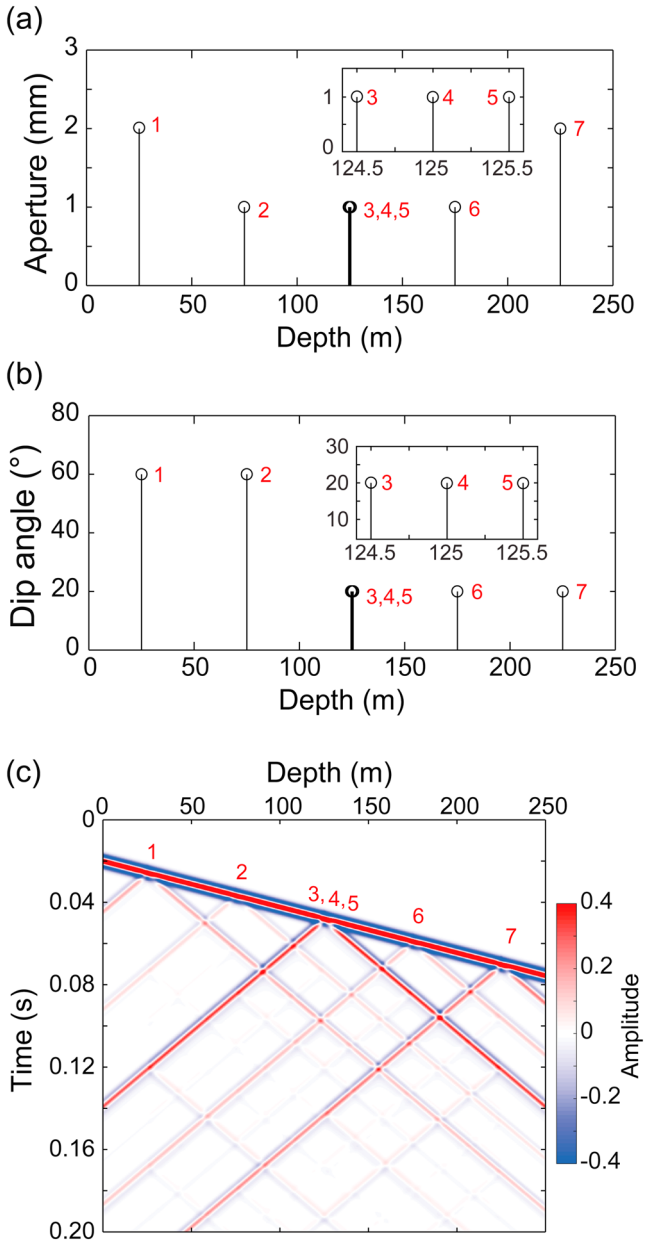

Figure 4. (a and b) Distribution of the position of fractures, fracture apertures, and dip angles which are used to derive the numerically modeled data in Figure 4c. Numbers in red show the fracture number: seven fractures are considered. (c) Numerically modeled total tube wavefield.

Figure 3c shows the effect of fracture aperture (L_0) when the dip angle is 40°. The amplitude ratio increases as the fracture aperture increases, which is also shown by Bakku et al. (2013) for the case of horizontal fractures.

4. Numerical Modeling

We use equation (1) in order to predict the complex signature of the tube wavefield due to closely spaced dipping fractures. The wavefield (p) can be obtained by numerically solving equation (1) using the known values of the incident pressure field (p_{inc}), the potential functions (ϕ_g and ϕ_s), and the reference Green's function ($\tilde{G}^{pq}$). Minato and Ghose (2017) show details about the numerical modeling procedure.

We first consider a simple model where seven fractures are located in an infinitely long borehole. The position of fractures and their properties (apertures and dip angles) are shown in Figures 4a and 4b. We consider the fracture apertures to be 1 or 2 mm (Figure 4a), and the dip angles to be 20° or 60° (Figure 4b). Furthermore, in order to see the effect of the closely spaced fractures, three fractures are located at 0.5 m spacing around 125 m depth (fracture number 3, 4, and 5 in Figures 4a and 4b and inset figures).

Figure 4c shows the numerically modeled total tube waves at 2 m depth intervals in a water-filled borehole. The borehole with a radius $R = 7.5$ cm is embedded in a homogeneous medium ($V_P = 4,500$ m/s, $V_S = 2,200$ m/s, $\rho = 2,500$ kg/m^3). We consider a normally incident plane P wave and an incident Ricker wavelet of 150 Hz center frequency with a maximum amplitude of 1. The large amplitudes in Figure 4c are clipped in order to make the later arrivals visible. The first arriving event in Figure 4c is the incident P wave. The tube waves are generated at fracture positions. The generated tube waves propagate upward and downward with the tube wave velocity, and they cause numerous reflections and transmissions. The generated amplitude is large for the large aperture (compare the tube waves generated at fracture number 1 and 2 in Figure 4c) and the small dip angle (compare the tube waves at fracture number 1 and 7). Furthermore, it is clear that the closely spaced multiple fractures at 125 m depth (the fracture number 3, 4, and 5) create larger amplitude than a single fracture with the same properties (compare the tube waves at 125 m depth and those at fracture number 6). This is because the generated tube waves interfere constructively resulting in an increase in the observed amplitude, which is shown earlier for horizontal fractures by Minato and Ghose (2017).

Next, we consider a more complex model. Figure 5a shows the numerically modeled total tube waves using the fracture distribution and the dip angles shown in Figure 5b. This fracture distribution is identical to that obtained in a controlled field experiment at a fault-damaged zone where open fractures are present in metamorphic rocks (see section 5). We consider the same properties (V_P, V_S, ρ, and R) for a fluid-filled borehole as those in the simple model (Figure 4c), but we consider boundary conditions at the top (z =0 m) and bottom (z = 250 m) of the borehole as, respectively, a traction-free boundary and a rigid boundary (Minato & Ghose, 2017). Note that the total tube wavefield are shown between 40 and 250 m depth (Figure 5a). The calculated tube wavefield indicates that the maximum tube-to-P wave amplitude ratio is around 3 (Figure 5a). This value of the amplitude ratio is larger than that for a single fracture with similar configurations (see values around 100–200 Hz in Figures 3a and 3b). This is because of the fact that tube waves originated from closely spaced multiple fractures interfere constructively, and this results in an increase in the observed amplitude, which is shown also in the simple model (Figure 4c).

Due to the close spacing of the multiple fractures, the generated tube waves interfere with each other, and it is difficult to isolate waves from one individual fracture. We propose a new approach for imaging the

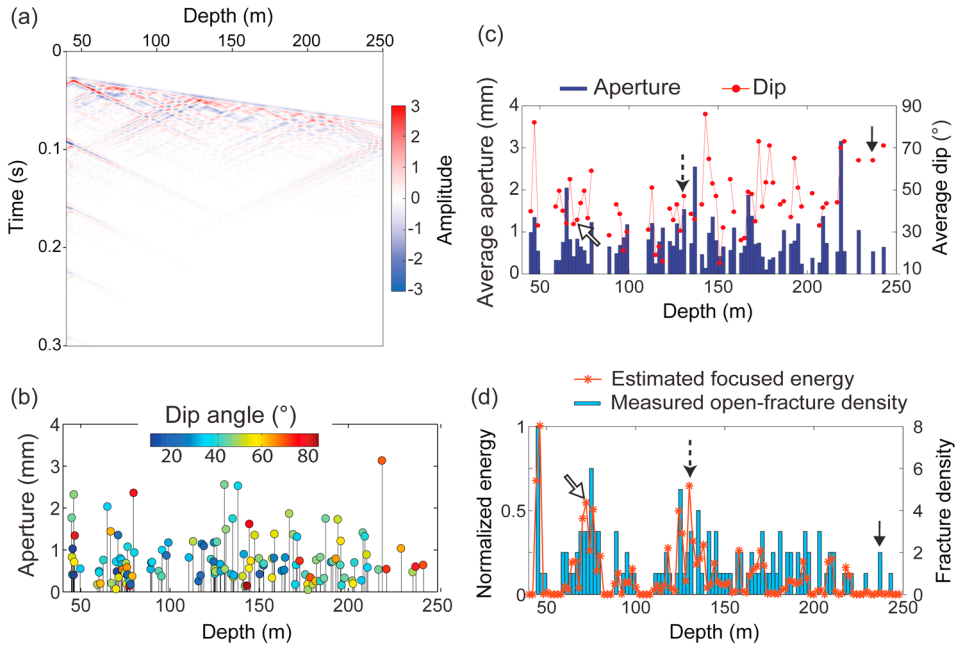

Figure 5. (a) Numerically modeled total tube wavefield for the fracture distribution shown in Figure 5b. (b) Distribution of the position of fractures, apertures, and dip angles. This distribution is obtained in a field experiment using OPTV. (c) Averaged (over 2 m depth range) apertures and dip angles calculated from Figure 5b at every 2 m interval. (d) The normalized energy obtained from the focusing analysis and the fracture density (2 m spacing) calculated from Figure 5b.

fractures using the total tube wavefield. To this end, we define a focusing operator h (Herman et al., 2000; Minato & Ghose, 2017) such that it satisfies $\delta(z' - z'') = \int_{-\infty}^{\infty} h(z'', z, \omega)\bar{G}^{pq}(z', z, \omega)\mathrm{d}z$. Application of this focusing operator to equation (1) results in

$$\int_{-\infty}^{\infty} h(z'', z, \omega)p_{\mathrm{scat}}(z, \omega)\mathrm{d}z = \phi_g(z'', \omega)p_{\mathrm{inc}}(z'', \omega) + \phi_s(z'', \omega)p_{\mathrm{scat}}(z'', \omega), \tag{9}$$

where $p_{\mathrm{scat}} = p - p_{\mathrm{inc}}$. Equation (9) indicates that the application of h to p_{scat} focuses the propagating tube waves to secondary source positions, which is useful to image the hydraulic fractures. Note that in practice, the focusing operator (h) can be numerically obtained from known values of the reference Green's function $\bar{G}^{pq}$ (Herman et al., 2000).

The result of the focusing analysis is controlled by the tube wavefield and the potential functions (right-hand side of equation (9). The potential functions contain information of fracture properties (e.g., aperture and dip angles). Therefore, the focusing analysis and equation (9) are useful to formulate the inverse problem in order to estimate fracture properties using the total wavefield. In this study, instead of solving the inverse problem, we consider the distribution of the normalized energy of the focused traces, that is, squared sum of the left-hand side of equation (9) for all frequencies followed by a normalization by the maximum value. Consideration of the normalized energy implies that we use relative amplitudes of the total tube wavefield. The normalized energy distribution has been shown to be useful in discussing the relative aperture distribution and the fracture density for horizontal fractures (Minato & Ghose, 2017).

Figure 5d shows the distribution of the normalized energy of the focused traces. Considering a 2 m receiver spacing, we calculate average apertures, average dip angles and fracture densities at 2 m intervals (Figures 5c and 5d) for the fracture distribution shown in Figure 5b. Between 40 and 150 m depth, the distribution of energy matches with the fracture density distribution (Figure 5d). This is because the majority of the fractures in these depths have similar apertures (0.2–1.0 mm) and dip angles (30°–50°). There is significant focused energy when a large number of fractures are located between two consecutive traces (2 m in this case). Furthermore, fractures with small dip angles give large energy than those with large dip angles. For example, the peak of the focused energy at 72 m depth (white arrow in Figure 5d) does not coincide precisely with the peak of the fracture density, mainly because the average dip angle of fractures at this depth is small (white arrow in Figure 5c) giving large generation amplitude. The focused energy at 238 m depth is small

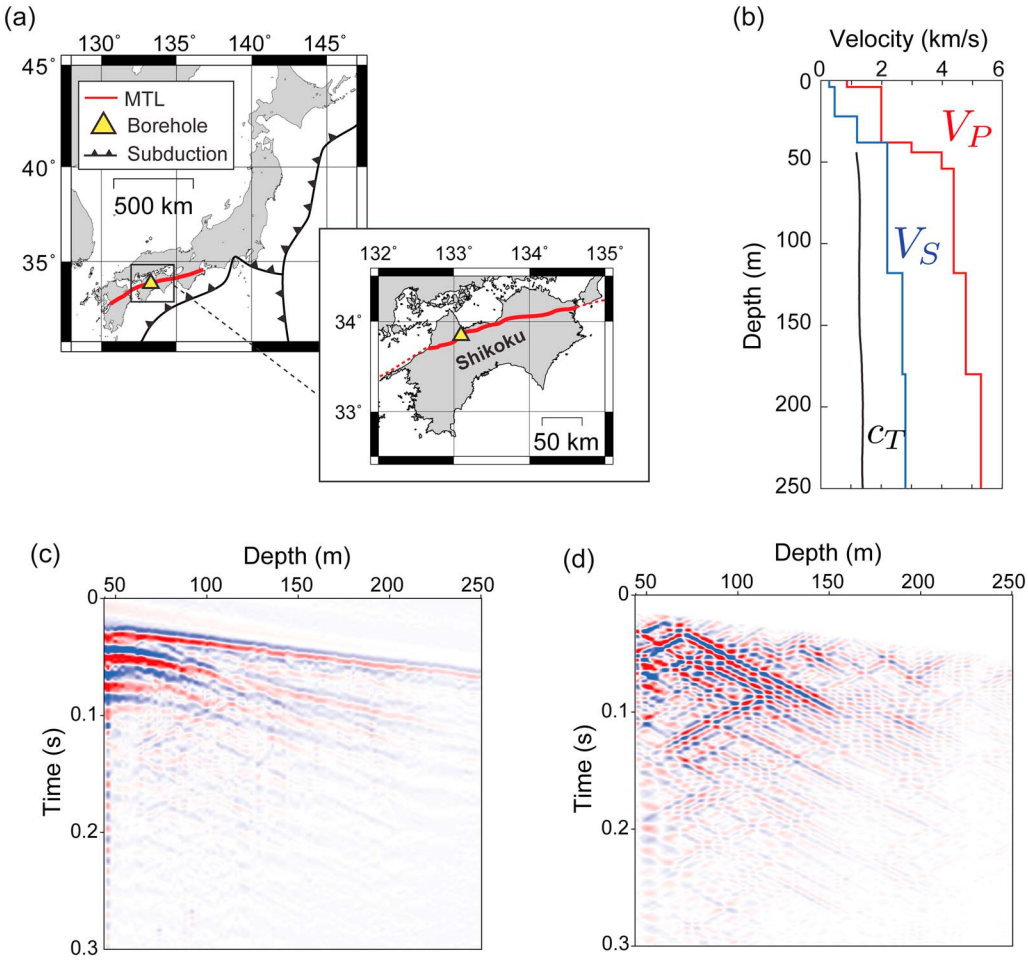

Figure 6. (a) MTL and the borehole location (triangle). (b) V_P and V_S from VSP data and the tube wave velocity from (d). (c) Vertical component of geophone data. (d) Estimated pressure data after removing the direct waves.

(black arrow in Figure 5d) due to the large dip angle of fractures at this depth (black arrow in Figure 5c). The second largest energy at 130 m depth (dashed arrow in Figure 5d) can be explained by a relatively large fracture density, large average aperture, and moderate dip angle around this depth (dashed arrow in Figure 5c). These results are in agreement with those expected from the generation amplitude ratio, discussed earlier (Figure 3).

5. Application to Field Data

5.1. Acquired Data and the Focusing Analysis

A near-offset VSP experiment was performed in a 250 m deep vertical borehole located on the Median Tectonic Line (MTL), Shikoku, Southwest Japan (Figure 6a). The MTL represents one of the most significant fault zones in Japan, associated with the motions of the subducting plates (Kubota & Takeshita, 2008). In this field, the high-pressure and low-temperature Sambagawa metamorphic rocks are unconformably overlain by the Late Cretaceous Izumi Group rocks (Ikeda et al., 2013). From core observation, we could identify the presence of the Sambagawa metamorphic rocks below 44 m depth, approximately. Figure 6b shows the estimated velocity structure from the field VSP experiment. From the optical borehole televiewer (OPTV), the positions of the open fractures and the thin cataclasite layers are known; these are permeable structures which can generate tube waves. In Appendix B, we show the examples of OPTV images. The distribution of the open fractures is shown in Figures 5b and 5c, and that of the cataclasite layers is shown in Figure 7a.

We used the vertical component of the geophone data due to a *P* wave source, at 2 m receiver spacing in the borehole, from 44 to 250 m depth (Figure 6c). The frequency content in the data is in 20–200 Hz range. The first arriving event shows the incident *P* wave, which is removed by spatially smoothing the data along

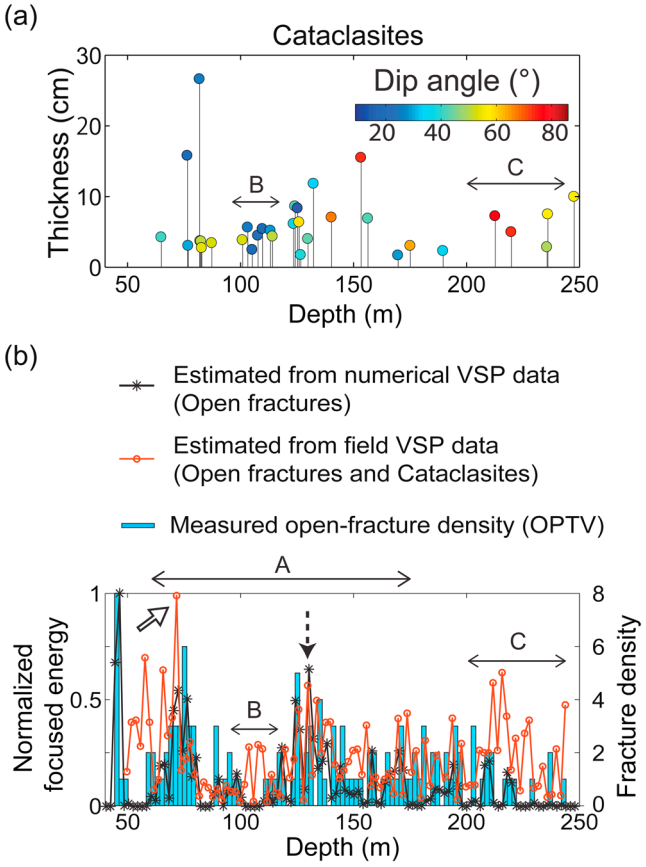

Figure 7. (a) Depth, thickness and dip angles of cataclasites, detected using OPTV. The same parameters for the open fractures are shown in Figures 5b and 5c. (b) Normalized energy distribution obtained from the focusing analysis applied to the numerically modeled VSP data (black line, same as the red line in Figure 5d) and to the field VSP data (red line). The fracture density derived for the open fractures (same as in Figure 5d) is also plotted here. The horizontal arrows mark three depth regions. A: the focused energy estimated on field data conforms with the measured open-fracture density and the energy estimated from the numerical data. B: the estimated focused energy on field data does not match with the measured open-fracture density and the cataclasite layers are dominant. C: the estimated focused energy on field data does not match with the fracture density and the energy is large compared to the numerical data.

the picked *P* wave travel time and subtracting the smoothed data from the total wavefield. After removing the incident wave, we estimate pressure field from the geophone data (see Appendix C for details). Geophone data are acquired using a single sensor housed in a borehole shuttle which is clamped to borehole wall. By using appropriate elastic parameters and solving the solid-fluid boundary conditions (Biot, 1952; Cheng & Toksöz, 1981), we find that the magnitude of radial displacement at the borehole wall is one order larger than that of vertical displacement, in the frequency range that we consider. However, we do not observe tube waves in the radial component of our data. This suggests that the vertical motion of the borehole fluid causes a vertical motion at the geophone due to the finite dimension of the measurement tool in the radial direction. In this regard, it is well known that a measurement tool behaves as a boundary which generates reflected tube waves (Hardage, 1981). Therefore, we estimate pressure field assuming that the data represent the particle motion of the measurement tool and considering the rigidity of the tool (Appendix C). The estimated maximum tube-to-*P* wave amplitude ratio is around 3 (see Figure C1b). This value of amplitude ratio is similar to the numerically predicted values (Figure 5a). Unfortunately, however, this does not fully preclude the effect of the borehole wall because including the motion of the borehole wall in the data can lead to large amplitudes in the estimated pressure field (Figure C1c), which may lead to large errors in amplitudes. Therefore, similar to the focusing analysis in the numerical modeling section, we consider only relative amplitudes of the estimated pressure field as shown in Figure C1b, for qualitatively investigating the effect of the fractures.

Figure 6d shows clearly the propagation of multiple tube waves. We estimate the tube wave velocity (c_T) by implementing the slant stacking technique (Yilmaz, 2001), which gives c_T around 1,300–1,400 m/s (Figure 6b). With p_{scat} from Figure 6d, we apply the focusing operator (equation (9)) derived from the estimated c_T, normalize the focused traces by the incident wave amplitude at each depth (Figure C1a), and then calculate the energy of the focused traces (Figure 7b).

5.2. Fracture Density Versus Focused Energy: Result on Field VSP and Numerical Data Sets

In this subsection, we discuss systematically the relation between the focused energy estimated from the field VSP data set, that from the numerical modeling, and the observed distribution of fracture density. Figure 7b shows the estimated focused energy from field VSP data (red line) and numerical data (black line). The numerically modeled data set is same as that shown in Figure 5d. The fracture density distribution is obtained for the open fractures (blue bars).

Note the good match between the estimated focused energy using our new methodology and the open-fracture density from OPTV, especially for the numerically modeled data (black line and blue bars in Figure 7b). As explained earlier, because the focused energy depends not only on fracture density but also on a few other parameters, for example, fracture aperture, dip, and compliance (see section 4), any difference between the calculated focused energy and the measured fracture density is understandable. When the same methodology (focusing analysis) is applied to the field VSP data set, we can see (red line in Figure 7b) that between 60 and 150 m depth (region A, marked by a horizontal arrow in Figure 7b), the energy distribution exhibits a trend which is quite close to the trend of the distribution of the open-fracture density. This trend also conforms with that of the focused energy obtained from numerically modeled data: the peak energy at 72 m (white arrow) and that at 130 m (dashed arrow) are in good agreement with those in the results on numerical data (Figure 7b). The depths where the focused energy in the field data does not match well with the measured open-fracture density (depth ranges B and C) are shown in Figure 7b. This discrepancy can be

attributed to the presence of cataclasite layers which are detected at these specific depth ranges (see B and C in Figure 7a). Furthermore, the focused energy in the field data at the depth range C is larger than that in the numerical data. This can be explained not only by the presence of the cataclasite layers but also by the large values of the fracture compliance (Z) at this depth. Note also that the effect of noise is likely to be larger at this depth (C) because the incident wave amplitude is smaller at greater depths (Figure C1a).

Although the trend of the focused energy distribution between 60 and 150 m depth (depth region A) is remarkably similar between the field data and the numerical data (red and black lines in Figure 7b), the relative amplitudes are different. Possible causes are (1) the effect of the cataclasite layers which is not considered in the numerical modeling, (2) the choice of different values for the fracture compliance (Z), (3) the finite dimension of the fractures (Bakku et al., 2013; Liang et al., 2017), and (4) insufficient focusing due to noise, the wrong values of tube wave velocity, and/or errors in estimating the pressure field from the geophone data.

Note also that although the thickness of the cataclasites is larger than that of the open fractures, they can be represented by the model developed in this study using effective hydraulic apertures. Tang and Cheng (1993) discussed tube wave scattering due to a poroelastic layer represented by a single fracture with aperture $\phi \times L$, where ϕ and L are, respectively, porosity and thickness of the layer. Their results imply that at low frequencies, the effective aperture requires to be lower than $\phi \times L$ in order to account for the viscous effects. Considering these discussions and a porosity around 10–20%, the contribution of the cataclasites to tube wave generation and scattering is expected to be in the same order of magnitude as that of the open fractures. It is possible to represent the cataclasites by a poroelastic layer model, for example, as in Tang and Cheng (1993) and Li et al. (1994), which has recently been tested for a horizontal fracture geometry (Minato et al., 2016).

6. Discussions

We have obtained the theoretical reflection coefficients of dipping fractures in section 3.2. We have shown that our extended model corresponds well to the foregoing studies of rigid fractures and that the theoretical reflection coefficients have correct limits at low and high frequencies. We have also obtained the effective generation amplitude including the effects of fracture dips in section 3.3. For a normal incidence P wave, the amplitude ratio decreases with the dip angle until around $\theta = 70°$, because the effect of the fracture deformation is more dominant than that of the length of the elliptical fracture-borehole boundary. When a dip angle is larger than 80°, the effective amplitude ratio rapidly increases with the dip angle (Figure 3b). This is possibly due to the effect of the large length of the elliptical fracture-borehole boundary. However, one needs to be careful as the proposed theory can contain large errors when the dip angle is close to 90° or when the vertical extent of the fracture in the borehole (L_1) is very large compared to the wavelength of tube waves. In this case, the assumption of the vertical symmetry in the flow rate (q_f) may fail. Alternatively, we may be able to numerically solve the equation of continuity in order to obtain q_f. Furthermore, when the vertical extent (L_1) is very large compared to the wavelength, the additional effect of the dynamic compression of ΔV needs to be considered in the mass conservation equation (equation (2)).

We have examined through numerical modeling the complex signatures of the tube wavefield due to dipping fractures in section 4. We have designed a focusing analysis, exploiting the interaction of the total tube wavefield in case of multiple dipping fractures. We have demonstrated that it is possible to image the dipping fractures. We have found that the large energy of the focused traces corresponds to the large fracture density, large apertures, and small dip angles.

The application to a field VSP data set from the Median Tectonic Line, Shikoku, Japan, shows evidence of tube wave propagation due to multiple fractures (section 5). For the first time it has been possible to relate the focused traces from the total tube wavefield to fracture density and other fracture properties (aperture and dip angle). We find evidence of tube wave generation and scattering at open fractures and the presence of thin cataclasites layers.

It should be noted that the focusing operator that we use depends only on the Green's function in the reference medium. Therefore, the focused traces and the normalized focused energy do not depend on the choice of the tube wave generation and scattering models. As we have shown, various models have been developed including the new model that we have presented in this research. The choice of an appropriate model is important when we interpret the focused traces, as we have demonstrated using our model. Furthermore,

it is possible to formulate the inverse problem to estimate fracture properties from the focused traces, which are represented by the tube wave generation and scattering potential functions (equation (9)). Note that in this case, we can implement any model developed so far.

7. Conclusions

We have presented here a major extension of our previous model representing interaction of the total tube wavefield in case of multiple, closely spaced fractures and have included the effects of the dip angle of the fractures. A new model for tube wave scattering and generation at dipping, parallel-wall, open fractures has been developed. We have proposed a focusing analysis in order to analyze the complex signatures of the tube wavefield. We have demonstrated this analysis using a numerically modeled data set and a field VSP data set obtained from the Median Tectonic Line in Japan.

The new approach that we have presented in this article allows measurement of in situ permeability due to multiple fractures. This will find key applications in numerous fields where monitoring the hydraulic properties of dipping fractures is needed, for example, in characterizing fluid paths during geological CO_2 storage, in geothermal field developments, in fault seal assessments in carbonate reservoirs, and in comprehending the role of fractures and fluids in tectonic processes.

Appendix A: Derivation of the Amplitude of the Generated Tube Waves Using the Ionov Boundary Condition

Using the tube wave generation model from Bakku et al. (2013) (equation (6) of Bakku et al. (2013) or equation (A7) of Minato and Ghose (2017)) and the equivalent circle approach (Tang & Cheng, 1993) that we explain in sections 3.2 and 3.3, the fluid pressure distribution (p_F) can be written as

$$p_F(r,\omega) = \left[p_t(\omega) - \frac{\rho_f Z \alpha_{\text{eff}}^2}{L_0}\sigma_0\right]\frac{H_0(\zeta r)}{H_0(\zeta \bar{R})} + \frac{\rho_f Z \alpha_{\text{eff}}^2}{L_0}\sigma_0, \tag{A1}$$

where r is the radial distance along a fracture, and we consider the Ionov boundary condition ($p_F(\bar{R},\omega) = p_t(\omega)$). Considering the dynamic fluid flow condition (Bakku et al., 2013; Tang & Cheng, 1989), we have the following relation:

$$q_f(r,\omega) = -\frac{i\omega L_0}{k_r^2 \alpha_f^2 \rho_f}\frac{\partial p_F}{\partial r}. \tag{A2}$$

Using equations (5), (6), (A1), and (A2), we obtain the tube wave generation amplitude (p_t^{Io}), using the Ionov boundary condition, as,

$$p_t^{\text{Io}}(\omega) = \frac{\sigma_0 \frac{L_e}{2\pi R}\frac{i\omega c_T}{k_r \alpha_f}\frac{\rho_f Z \alpha_{\text{eff}}}{R}\frac{H_1(\zeta\bar{R})}{H_0(\zeta\bar{R})}}{1 + i\omega\frac{\rho_f c_T}{2} \times \left(2\zeta\frac{\bar{R}}{R^2}\frac{L_0}{k_r^2\alpha_f^2\rho_f}\frac{H_1(\zeta\bar{R})}{H_0(\zeta\bar{R})}\right)}. \tag{A3}$$

Equation (A3) is identical to equation (8) which is derived assuming the Beydoun boundary condition and that additional scattering is taking place immediately after generation.

Appendix B: Example of Images From the Optical Borehole Televiewer (OPTV)

We obtain the distribution of the open fractures (Figure 5b) and that of the cataclasite layers (Figure 7a) from OPTV images. The apertures of the open fractures are estimated by picking the apparent apertures at every 30° azimuth. Averaged values are then corrected for dip angles to obtain the true apertures. Dip and strike angle are estimated by fitting the sine curvature on the OPTV images. Similarly, the thicknesses of the cataclasite layers are estimated by picking the upper and lower surface of the layers. The dip angles of the cataclasite layers are then obtained by averaging those of the upper and lower surfaces. Figures B1 and B2 show, respectively, the examples of the OPTV images of the open fractures and the cataclasite layers.

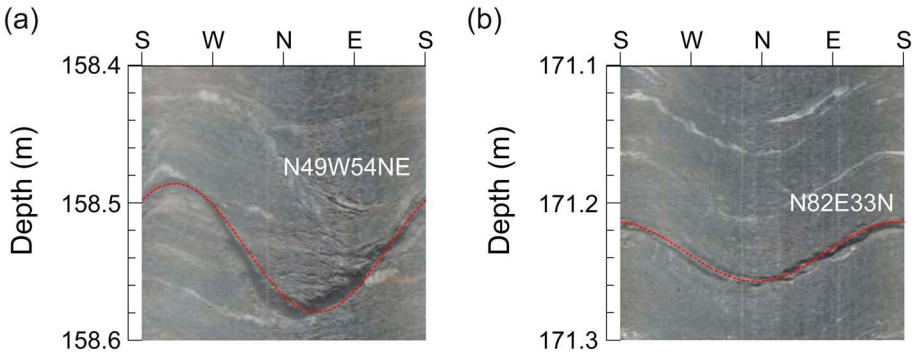

Figure B1. Examples of open fractures detected in OPTV images. (a) At 158.5 m depth; average aperture is 1.4 mm. (b) At 171.2 m depth; average aperture is 1.3 mm. The red dashed lines show the dip and strike angles of the structure.

Appendix C: Estimating Pressure Field From the Geophone Data

In the field data, we obtain the spatially smoothed traces by filtering the vertical component of geophone records, which contain the vertical particle velocity (v_z) of the direct *P* wave. We assume that the smoothed traces includes v_z at the borehole wall and estimate the fluid pressure in the borehole (p) due to the incident *P* wave.

Using the low-frequency approximation of the axisymmetric waves in a fluid-filled borehole due to an incident plane *P* wave (Schoenberg, 1986), we obtain the relation between the vertical particle velocity at the borehole wall (v_z) and the pressure in the borehole (p):

$$p = V \frac{\rho_f V_P c_T^2}{V_S^2} \frac{1 - 2V_S^2 V_P^{-2} \cos^2 \varphi}{1 - c_T^2 V_P^{-2} \cos^2 \varphi}, \qquad \text{(C1)}$$

$$v_z = V \cos \varphi,$$

where V is the amplitude of the incident *P* wave, φ is the incidence angle ($\varphi = \cos^{-1}(\hat{z}_b \cdot \hat{k})$, see Figure 1b), and we assume that p is the value at the center of the borehole.

Using equation (C1), we obtain the pressure field in the borehole from the smoothed traces. Figure C1a shows the estimated pressure field of the normally incident *P* wave after muting around direct arrivals. Note that the pressure field (Figure C1a) is scaled by the maximum amplitude of all traces.

After subtracting the smoothed traces from the total wavefield, we obtain the vertical particle velocity of the tube wavefield. In order to estimate the tube wave pressure field, we follow a simple approach to consider

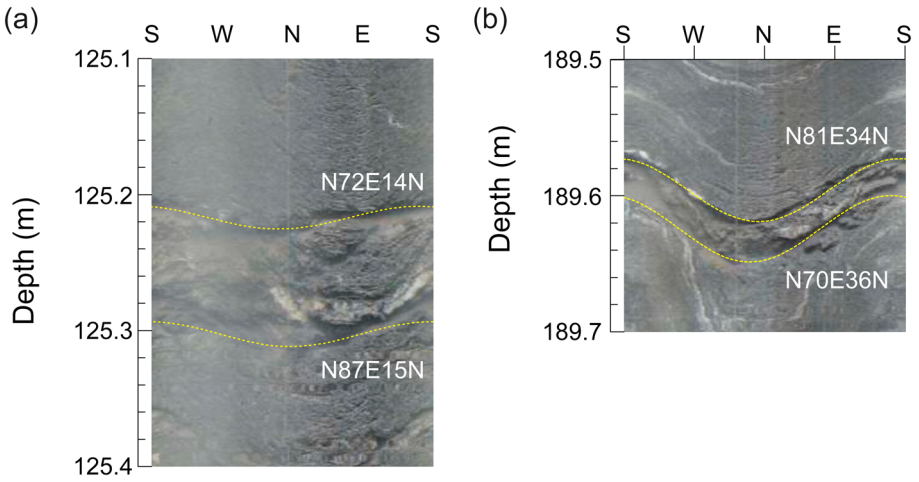

Figure B2. Examples of thin layers of cataclasite detected in OPTV images. (a) At 125.2 m depth; average thickness is 8.3 cm. (b) At 189.6 m depth; average thickness is 2.3 cm. The yellow dashed lines show the dip and strike angles of the upper and lower surface of the structure.

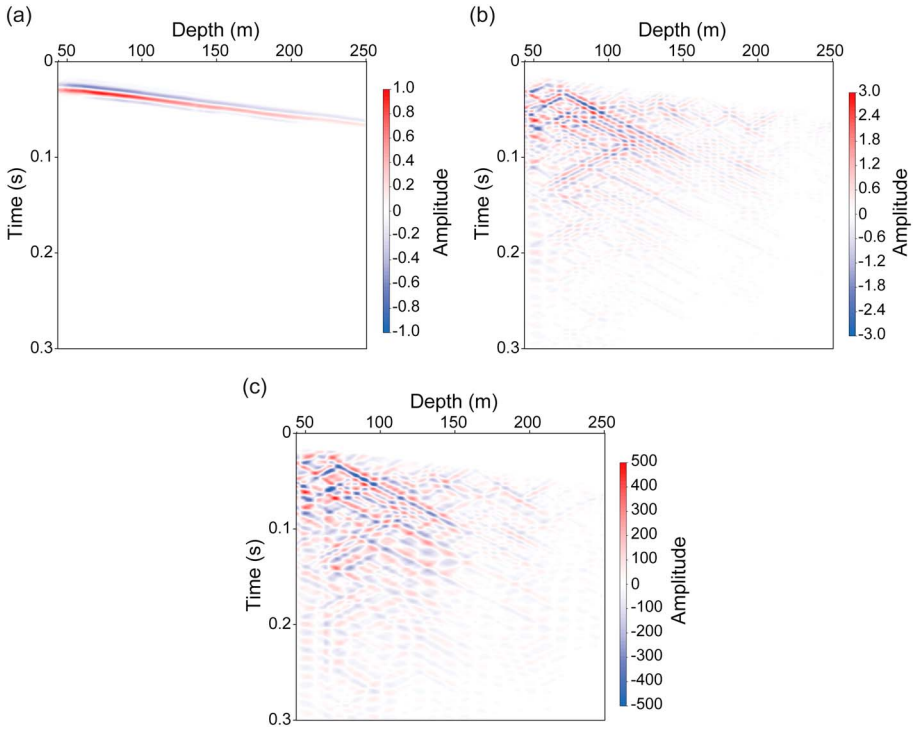

Figure C1. (a) Estimated incident pressure field. (b) Estimated tube wave pressure field assuming that the geophone data represent the motion of the measurement tool due to the vertical fluid motion. (c) Estimated tube wave pressure field assuming that the geophone data represent the motion of the borehole wall.

the interaction between the borehole fluid and the measurement tool. We consider following assumptions: (1) a vertical motion of tube wave causes a vertical motion at the measurement tool due to the finite dimension of the tool in the radial direction, (2) the measurement tool has similar elastic properties to those of the formation because the tool is clamped to the borehole wall, and (3) the tool behaves as an elastic half space. The third assumption implies one-dimensional wave propagation and that we ignore the finite length of the measurement tool.

We consider that a downgoing incident tube wave generates reflected and transmitted wave at a boundary between the borehole fluid and the elastic half space (measurement tool). The vertical displacement of the incident, reflected, and transmitted waves are written as, $u_z^i = Ae^{ik_T z - i\omega t}$, $u_z^r = Be^{-ik_T z - i\omega t}$, and $u_z^t = Ce^{ik_P z - i\omega t}$, respectively. Here $k_T = \omega/c_T$ is the wave number of tube wave, $k_P = \omega/V_P$ is the longitudinal wave number of the elastic half space, and A, B, and C are amplitude coefficients. By solving at the boundary the continuity equation for both displacement and stress, we obtain the following relation between the amplitude of the incident wave (A) and that of the transmitted wave (C):

$$A = \frac{Z_T + Z_P}{2Z_T} C, \tag{C2}$$

where $Z_T = \rho_f c_T$ and $Z_P = \rho V_P$.

We assume that the fluid pressure (p) and the vertical displacement (u_z) at the measurement tool are represented by a superposition of upgoing and downgoing waves as,

$$\begin{aligned} p &= A^d e^{ik_T z} + A^u e^{-ik_T z}, \\ u_z &= C^d e^{ik_P z} + C^u e^{-ik_P z}, \end{aligned} \tag{C3}$$

where we omit the factor $e^{-i\omega t}$ for brevity, $A^{d,u}$ and $C^{d,u}$ are the amplitudes, and the superscripts indicate upgoing wave (u) or downgoing wave (d). We assume that the measurement tool behaves as an elastic half space

for each upgoing and downgoing wave mode. Using equations (C2) and (C3), after a simple algebra we obtain the following relation at the receiver position:

$$p = -\frac{V_P}{2}(Z_T + Z_P)\frac{\partial u_z}{\partial z}. \tag{C4}$$

Approximating $\partial u_z/\partial z$ as $(-i\omega)^{-1}\left\{v_z(z+\Delta z) - v_z(z)\right\}/\Delta z$, where $v_z(z)$ indicates vertical particle velocity (geophone data), we can estimate the pressure field p from the geophone data. The estimated pressure field is shown in Figure C1b. Note that the pressure field is scaled by the maximum amplitude in the direct pressure field (Figure C1a), so that we can see the tube-to-*P* wave amplitude ratio.

Finally, Figure C1c shows the estimated pressure field assuming that the geophone data contain the vertical motion of the borehole wall. For this purpose, we use the analytical solutions for the motion of borehole fluid and that of the borehole wall, which are derived from the wave equation in cylindrical coordinates and the solid-fluid boundary conditions (e.g., Biot, 1952; Cheng & Toksöz, 1981). See supporting information for more details. The result shows that the amplitude of the estimated pressure field is much larger than that obtained considering the finite dimension of the tool in the radial direction (compare Figures C1b and C1c). This is because a large pressure is required to cause a vertical displacement at the borehole wall due to the discontinuity of shear stress at the solid-fluid boundary. We have also found that the radial displacement at the borehole wall is expected to be larger than the vertical displacement. As explained in the main text, we do not, however, identify tube waves in the radial component of our data, which partly supports the conjecture that the effect of the finite dimension of the tool in the radial direction is dominant in our data.

Acknowledgments
Ownership of the field seismic data and OPTV images remains with Shikoku Electric Power Co. Inc. and Shikoku Research Institute Inc. The field seismic data used in this study may be available by contacting Shikoku Research Institute Inc. The fracture distribution used to generate the synthetic data is provided in Table S1 in the supporting information. This work is supported by the Netherlands Research Centre for Integrated Solid Earth Science (ISES). We thank Shikoku Electric Power Co. Inc. and Shikoku Research Institute Inc. for providing the field data used in this study. This work is partially supported by JSPS (15H01143 and 17H05318).

References

Ashour, A. S. (2000). Wave motion in a viscous fluid-filled fracture. *International Journal of Engineering Science*, *38*(5), 505–515. https://doi.org/10.1016/S0020-7225(99)00045-2

Bakku, S. K., Fehler, M., & Burns, D. (2013). Fracture compliance estimation using borehole tube waves. *Geophysics*, *78*(4), D249–D260. https://doi.org/10.1190/geo2012-0521.1

Beydoun, W., Cheng, C., & Toksöz, M. (1985). Detection of open fractures with vertical seismic profiling. *Journal of Geophysical Research*, *90*(B6), 4557–4566. https://doi.org/10.1029/JB090iB06p04557

Biot, M. (1952). Propagation of elastic waves in a cylindrical bore containing a fluid. *Journal of Applied Physics*, *23*(9), 997–1005. https://doi.org/10.1063/1.1702365

Biot, M. (1956). Theory of propagation of elastic waves in a fluid-saturated porous solid—II: Higher frequency range. *Journal of the Acoustical Society of America*, *28*(2), 179–1191. https://doi.org/10.1121/1.1908241

Chang, S. K., Liu, H. L., & Johnson, D. L. (1988). Low-frequency tube waves in permeable rocks. *Geophysics*, *53*(4), 519–527. https://doi.org/10.1190/1.1442483

Cheng, C. H., & Toksöz, M. N. (1981). Elastic wave propagation in a fluid-filled borehole and synthetic acoustic logs. *Geophysics*, *46*(7), 1042–1053. https://doi.org/10.1190/1.1441242

Cicerone, R. D., & Toksöz, M. N. (1995). Fracture characterization from vertical seismic profiling data. *Journal of Geophysical Research*, *100*(B3), 4131–4148. https://doi.org/10.1029/94JB02982

Ferrazzini, V., & Aki, K. (1987). Slow waves trapped in a fluid-filled infinite crack: Implication for volcanic tremor. *Journal of Geophysical Research*, *92*(B9), 9215–9223. https://doi.org/10.1029/JB092iB09p09215

Hardage, B. (1981). An examination of tube wave noise in vertical seismic profiling data. *Geophysics*, *46*(6), 892–903. https://doi.org/10.1190/1.1441228

Hardin, E., Cheng, C., Paillet, F., & Mendelson, J. (1987). Fracture characterization by means of attenuation and generation of tube waves in fractured crystalline rock at Mirror Lake, New Hampshire. *Journal of Geophysical Research*, *92*(B8), 7989–8006. https://doi.org/10.1029/JB092iB08p07989

Herman, G. C., Milligan, P. A., Dong, Q., & Rector, J. W. (2000). Analysis and removal of multiply scattered tube waves. *Geophysics*, *65*(3), 745–754. https://doi.org/10.1190/1.1444773

Hornby, B., Johnson, D., Winkler, K., & Plumb, R. (1989). Fracture evaluation using reflected Stoneley-wave arrivals. *Geophysics*, *54*(10), 1274–1288. https://doi.org/10.1190/1.1442587

Hornby, B. E., Luthi, S. M., & Plumb, R. A. (1992). Comparison of fracture apertures computed from electrical borehole scans and reflected Stoneley waves: An integrated interpretation. *The Log Analyst*, *33*(01), 50–66.

Ikeda, M., Kato, S., Nishizaka, N., Ohno, Y., Matsuo, K., & Kishimoto, M. (2013). Magnetotelluric imaging of the Median Tectonic Line in western Shikoku, southwest Japan: Implications of the fault-related low-resistivity zone. *Tectonophysics*, *601*, 78–86. https://doi.org/10.1016/j.tecto.2013.04.026

Ionov, A. M. (2007). Stoneley wave generation by an incident *P*-wave propagating in the surrounding formation across a horizontal fluid-filled fracture. *Geophysical Prospecting*, *55*(1), 71–82. https://doi.org/10.1111/j. 1365-2478.2006.00577.x

Kiguchi, T., Ito, H., Kuwahara, Y., & Miyazaki, T. (2001). Estimating the permeability of the Nojima Fault Zone by a hydrophone vertical seismic profiling experiment. *Island arc*, *10*(3–4), 348–356. https://doi.org/10.1111/j.1440-1738.2001.00333.x

Koorneev, V. (2008). Slow waves in fractures filled with viscous fluid. *Geophysics*, *73*(1), N1–N7. https://doi.org/10.1190/1.2802174

Kostek, S., Johnson, D. L., Winkler, K. W., & Hornby, B. E. (1998). The interaction of tube waves with borehole fractures, Part II: Analytical models. *Geophysics*, *63*(3), 809–815. https://doi.org/10.1190/1.1444392

Kubota, Y., & Takeshita, T. (2008). Paleocene large-scale normal faulting along the Median Tectonic Line, western Shikoku, Japan. *Island Arc*, *17*, 129–151. https://doi.org/10.1111/j.1440-1738.2007.00607.x

Li, Y., Rabbel, W., & Wang, R. (1994). Investigation of permeable fracture zones by tube-wave analysis. *Geophysical Journal International*, *116*(3), 739–753. https://doi.org/10.1111/j.1365-246x.1994.tb03294.x

Liang, C., O'Reilly, O., Dunham, E. M., & Moos, D. (2017). Hydraulic fracture diagnostics from Krauklis-wave resonance and tube-wave reflections. *Geophysics*, *82*(3), D171–D186. https://doi.org/10.1190/geo2016-0480.1

Lipovsky, B. P., & Dunham, E. M. (2015). Vibrational modes of hydraulic fractures: Inference of fracture geometry from resonant frequencies and attenuation. *Journal of Geophysical Research: Solid Earth*, *120*, 1080–1107. https://doi.org/10.1002/2014JB011286

Minato, S., & Ghose, R. (2016). AVO inversion for a non-welded interface: Estimating compliances of a fluid-filled fracture. *Geophysical Journal International*, *206*(1), 56–62. https://doi.org/10.1093/gji/ggw138

Minato, S., & Ghose, R. (2017). Low-frequency guided waves in a fluid-filled borehole: Simultaneous effects of generation and scattering due to multiple fractures. *Journal of Applied Physics*, *121*(10), 104902. https://doi.org/10. 1063/1.4978250

Minato, S., Ghose, R., Tsuji, T., Ikeda, M., & Onishi, K. (2016). Modeling and imaging of multiply generated and scattered tube waves due to multiple hydraulic fractures. *SEG Technical Program Expanded Abstracts*, *35*, 682–687.

Nagy, P. (1992). Ultrasonic classification of imperfect interfaces. *Journal of Nondestructive Evaluation*, *11*(3–4), 127–139. https://doi.org/10.1007/BF00566404

Pyrak-Nolte, L., Myer, L., & Cook, N. (1990). Transmission of seismic waves across single natural fractures. *Journal of Geophysical Research*, *95*(B6), 8617–8638. https://doi.org/10.1029/JB095iB06p08617

Rokhlin, S. I., & Wang, Y. J. (1991). Analysis of boundary conditions for elastic wave interaction with an interface between two solids. *Journal of the Acoustical Society of America*, *89*(2), 503–515. https://doi.org/10.1121/1.400374

Schoenberg, M. (1980). Elastic wave behavior across linear slip interfaces. *Journal of the Acoustical Society of America*, *68*(5), 1516–1521. https://doi.org/10.1121/1.385077

Schoenberg, M. (1986). Fluid and solid motion in the neighborhood of a fluid-filled borehole due to the passage of a low-frequency elastic plane wave. *Geophysics*, *51*(6), 1191–1205.

Segall, P., & Pollard, D. D. (1983). Nucleation and growth of strike slip faults in granite. *Journal of Geophysical Research*, *88*(B1), 555–568. https://doi.org/10.1029/JB088iB01p00555

Tang, X. M., & Cheng, C. (1989). A dynamic model for fluid flow in open borehole fractures. *Journal of Geophysical Research*, *94*(B6), 7567–7576. https://doi.org/10.1029/JB094iB06p07567

Tang, X. M., & Cheng, C. (1993). Borehole Stoneley wave propagation across permeable structures. *Geophysical Prospecting* , *41*(2), 165–187. https://doi.org/10.1111/j.1365-2478.1993.tb00864.x

Tezuka, K., Cheng, C. H. A., & Tang, X. M. (1997). Modeling of low-frequency Stoneley-wave propagation in an irregular borehole. *Geophysics*, *62*(4), 1047–1058. https://doi.org/10.1190/1.1444206

Wapenaar, K. (2007). General representations for wavefield modeling and inversion in geophysics. *Geophysics*, *72*(5), SM5–SM17. https://doi.org/10.1190/1.2750646

White, J. E. (1983). *Underground sound: Application of seismic waves* (Vol. 253). Amsterdam, New York: Elsevier.

Wibberley, C. A., & Shimamoto, T. (2003). Internal structure and permeability of major strike-slip fault zones: The Median Tectonic Line in Mie Prefecture, Southwest Japan. *Journal of Structural Geology*, *25*(1), 59–78. https://doi.org/10.1016/S0191-8141(02)00014-7

Worthington, M., & Lubbe, R. (2007). The scaling of fracture compliance. *Geological Society London Special Publications*, *270*(1), 73–82. https://doi.org/10.1144/GSL.SP.2007.270.01.05

Yilmaz, O. (2001). *Seismic data analysis* (Vol. 10, 2nd ed.). Tulsa, OK: Society of Exploration Geophysicists. https://doi.org/10.1190/1.9781560801580